Analyzing the Human Liver Vascular Architecture by Combining Vascular Corrosion Casting and Micro-CT Scanning: a Feasibility Study

Short running page heading

"Analyzing the Human Liver Vascular Architecture"

Charlotte Debbaut[1], Patrick Segers[1], Pieter Cornillie[2], Christophe Casteleyn[3], Manuel Dierick[4], Wim Laleman[5], Diethard Monbaliu[6]

[1]Biofluid, Tissue and Solid Mechanics for Medical Applications, Institute Biomedical Technology, Ghent University. De Pintelaan 185 – Block B, B-9000 Gent, Belgium (charlotte.debbaut@ugent.be; patrick.segers@ugent.be)
Telephone: 003293313137

[2]Department of Morphology, Faculty of Veterinary Medicine, Ghent University. Salisburylaan 133, B-9820 Merelbeke, Belgium (pieter.cornillie@ugent.be)
Telephone: 003292647722

[3]Laboratory of Applied Veterinary Morphology, Embryology & Pathology, Department of Veterinary Sciences, Faculty of Pharmaceutical, Biomedical and Veterinary Sciences, University of Antwerp. Universiteitsplein 1, 2610 Wilrijk, Belgium (christophe.casteleyn@ua.ac.be)

Telephone: 003232652821

[4]UGCT, Department of Physics and Astronomy, Ghent University. Proeftuinstraat 86, B-9000 Gent, Belgium (manuel.dierick@ugent.be)

Telephone: 003292646611 / 003292646532

[5] Hepatology, University Hospitals Leuven, & department Development and Regeneration, KU Leuven. Herestraat 49, B-3000 Leuven, Belgium (wim.laleman@uzleuven.be)

Telephone: 003216344299

[6]Abdominal Transplant Surgery, University Hospitals Leuven, & department of Microbiology and Immunology, KU Leuven. Herestraat 49, B-3000 Leuven, Belgium (diethard.monbaliu@uzleuven.be)

Telephone: 003216344222

List of abbreviations

HA	Hepatic Artery / Hepatic Arterial
PV	Portal Vein / Portal Venous
HV	Hepatic Vein / Hepatic Venous
CT	Computer Tomography
DICOM	Digital Imaging and Communications in Medicine
VCI	Vena Cava Inferior
r	Radius

l	Length
n	Number of vessels
R^2	Coefficient of determination
x, f	Generation number

There is no conflict of interest.

Summary/Abstract

Introduction: Although a full understanding of the hepatic circulation is one of the keys to successfully perform liver surgery and to elucidate liver pathology, relatively little is known about the functional organisation of the liver vasculature. Therefore, we materialized and visualized the human hepatic vasculature at different scales and performed a morphological analysis by combining vascular corrosion casting with novel micro-CT and image analysis techniques.

Methods: A human liver vascular corrosion cast was obtained by simultaneous resin injection in the hepatic artery and portal vein. A high resolution (110 µm) micro-CT scan of the total cast allowed gathering detailed macrovascular data. Subsequently, a mesocirculation sample (starting at generation 5; 88 x 68 x 80 mm^3) and a microcirculation sample (terminal vessels including sinusoids; 2.0 x 1.5 x 1.7 mm^3) were dissected and imaged at a 71 µm and 2.6 µm resolution, respectively.

Results: Segmentations and 3D reconstructions allowed quantifying the macro- and mesoscale branching topology and geometrical features of hepatic arterial, portal venous and hepatic venous trees up to 13 generations (radii ranging from 13.2 mm to 80 µm; lengths from 74.4 mm to 0.74 mm), as well as microvascular characteristics (mean sinusoidal radius of 6.63 µm).

Conclusions: Combining corrosion casting and micro-CT imaging allows quantifying the branching topology and geometrical features of hepatic trees using a multiscale approach from the macro- down to the microcirculation. This may lead to novel insights into liver circulation, such as internal blood flow distributions and anatomical consequences of pathologies (e.g. cirrhosis).

Keywords: morphology, hepatic vasculature, image processing, 3D reconstruction, tree analysis

Introduction

The liver is a fascinating but complex multifunctional organ, characterized by its intricate vascular architecture. Compared to other organs, the liver's vasculature is unique due to the two blood supplies. Traditionally, the hepatic artery (HA) is regarded to supply the liver with oxygenated blood. The portal vein (PV) collects partially deoxygenated blood from the intestinal tract including spleen and pancreas. HA and PV blood mixes in the sinusoids, the hepatic microcirculation, often portrayed as a lattice of small vessels in between rows of hepatocytes, determining the smallest functional unit or liver lobule. Blood subsequently leaves liver lobules through central veins and eventually drains into the vena cava inferior (VCI) via the hepatic venous system (HV) (Roskams et al., 2007). All vascular trees as well as the microcirculation have their own morphological and functional characteristics. Together, they determine the hepatic hemodynamic behavior, such as the arterial buffer response (Eipel et al., 2010) or less physiologic phenomena such as flow competition between the HA and PV (Monbaliu et al., 2012).

The clinical relevance to understand the exact hepatic vascular anatomy is illustrated by the disturbed vascular architecture in case of liver pathology, such as cirrhosis with fibrosis (overproduction of extracellular matrix), regenerative nodules, increased vascular resistance, neo-angiogenesis and vascular remodeling leading to portal hypertension and intrahepatic shunt vessels (Anthony et al., 1978, Chen et al., 2009, Thabut and Shah, 2010). Moreover, the hepatic vasculature is subject to intraspecies anatomical differences, relevant for transplantation. Patient-specific analysis of the hepatic vascular topology through computed tomography (CT) and

magnetic resonance angiography may facilitate surgical planning and improve its outcome (Mutter et al., 2009, Selle et al., 2002, Yamanaka et al., 2006). Furthermore, topology information and geometrical characteristics may be fed to numerical models to simulate hepatic hemodynamics, useful to model e.g. surgical procedures or the performance of new preservation techniques for transplant livers (e.g. machine perfusion) (Debbaut et al., 2011, Bonfiglio et al., 2010, Rani et al., 2006, Ricken et al., 2010, Debbaut et al., 2012b, Debbaut et al., 2012a).

Morphological analysis of vascular trees in different organs and species is not new (e.g. rodent pulmonary trees (Gomes and Bates, 2002), mouse placental arteries (Rennie et al., 2011), human coronary arteries (Finet et al., 2007), mouse kidneys (Wagner et al., 2011)). However, to our knowledge, only a few papers were published on the liver's vasculature. Op Den Buijs et al. (Op Den Buijs and Ritman, 2006) classified the PV tree of the rat liver, but not the HA or HV tree. Selle et al. (Selle et al., 2002) focused on analyzing the macrocirculation for surgical planning based on vascular territories. We previously performed studies on modeling liver perfusion based on the macrovessel architecture of the human (Debbaut et al., 2011) and rat liver (Francque et al., 2012, Debbaut et al., 2012a). A larger number of studies has been published on liver microcirculation using for example microscopy, histological techniques (Teutsch et al., 1999, Ekataksin and Wake, 1991, Ekataksin and Wake, 1997, Greenway and Stark, 1971, Matsumoto and Kawakami, 1982, Matsumoto et al., 1979, McCuskey, 1966, McCuskey and Reilly, 1993, Rappaport et al., 1954), or performing 3D reconstructions by registering 2D serial cryosections as done by Teutsch et al. (Teutsch, 2005).

Until now, the total spectrum of the human liver vascular architecture has not been analyzed yet in a systematic way on single liver samples. Therefore, the aim of this study was to analyze the complete human liver vascular architecture using a combination of vascular corrosion casting, micro-CT scanning and image processing. Hereby, a novel multiscale approach was applied to consecutively analyze the macro-, meso- and microcirculation.

Materials and methods

In this study, a human liver was used after being discarded for transplantation due to failed reallocation. The protocol conforms to the ethical guidelines of the 1975 Declaration of Helsinki, and was approved by the Ethical Committee of the University Hospitals Leuven, Belgium, and by the Belgian Liver and Intestine Committee as foreseen by the initial protocol.

Vascular corrosion casting

After hepatectomy, the liver (weight ± 1.9 kg) was connected to a machine perfusion preservation device (Organ Recovery Systems, Zaventem, Belgium) during a 24h period, and was continuously perfused at 4-6°C with pressure-control through the HA (25 mmHg; unlimited flow) and PV (7 mmHg; flow limitation of 300 ml/min). The pressure-controlled feedback system, incorporated in the perfusion machine, ensured that perfusion pressures did not exceed the maximum pressure settings. Machine perfusion allowed preserving the vasculature and parenchyma and keeping the blood vessels open whilst preparing the necessary logistics. Subsequently, the liver was prepared for the vascular corrosion casting procedure by cannulation of the HA, PV as well as the VCI. Casting resin was prepared by mixing Batson's #17 monomer solution, catalyst and promoter (Polysciences, Warrington, USA) with monomeric methyl methacrylate (Merck, Darmstadt, Germany) and color dyes (red and blue for the HA and PV, respectively). In addition, barium sulfate (50 mg/ml; Micropaque, Delpharm, France) was added to the HA injection to amplify the contrast between arterial and venous vessels on CT images, facilitating to distinguish different contributing vessels. The HA and PV were simultaneously and manually injected until the resin emerged sufficiently from the VCI. Afterwards, inlet and outlet

vessels were clamped to avoid resin leakage during polymerization of the injected mixture (approximately two hours). Next, the liver was macerated in a potassium hydroxide bath (approximately two days). More detailed information on the vascular corrosion procedure is available in (Debbaut et al., 2011).

Micro-CT imaging

Macrocirculation

The resulting human liver cast (Fig. 1a) was imaged in globo to acquire data of the first blood vessel generations, being a similar number of generations as obtained with traditional angiography techniques (macrocirculation; Fig. 1a). This was done using a state-of-the-art in-house developed high resolution micro-CT scanner (Fig. 1d). Two thousand images were recorded during a 360° rotation of the cast. The image dataset (resolution of 102 µm) was reconstructed with Octopus software (Ghent University, Gent, Belgium) and converted to the DICOM format. More information on the scanning procedure is available in (Debbaut et al., 2011).

Mesocirculation

A smaller sample (wedge-shaped; approximately 88 mm x 68 mm x 80 mm) was dissected from the inferior part of the right lobe (Fig. 1a-b) to investigate the morphology of vessel generations distal to the macrocirculation. This sample was imaged at a resolution of 71 µm.

Microcirculation

Thirdly, a microvascular sample (approximately 2.0 mm x 1.5 mm x 1.7 mm) was dissected from the superior part of the right lobe to study the smallest vessels of the liver (Fig. 1c). To assure that the sinusoids were filled during casting, this sample was imaged by scanning electron microscopy (Fig. 1c). Afterwards, the sample was imaged using the micro-CT scanner at a 2.6 µm resolution.

Image processing and vascular architecture analysis

Macrocirculation

The resulting micro-CT dataset was processed using Mimics (Materialise, Leuven, Belgium). The vascular trees were segmented based on the gray values of the images. Separating arterial from venous vessels was straightforward due to the arterial contrast agent. It was, however, challenging to segment the PV and HV trees (having similar gray values), which were manually separated at locations where they touched each other. Therefore, each vascular tree was followed starting at the first generation vessel going down to smaller vessels. When a touching vessel was detected, it was separated by removing the pixel(s) of the connection. After segmentation, a 3D reconstruction of each tree was calculated.

After image processing, the vascular tree centerlines were calculated using the centerline algorithm in Mimics. Using the concept of blood vessel generations, the centerlines were used to determine the branching topology and geometrical features of all vascular trees. This was done by classifying vessels based on their branching pattern (see (Debbaut et al., 2011) for more detailed information), being either *n*-furcations (parent vessels splitting in *n* similar daughter vessels (dichotomous bifurcations when *n=2*) or monopodial vessels (small side branches coming of parent vessels at an angle close to 90°) (Gordon et al., 2007). Hereby, the inlet vessel of each vascular tree is assigned to generation 1. Daughter vessels have higher generation numbers than

their parent vessel. For instance, if a generation *n* vessel splits into two daughter vessels with a similar smaller diameter, the daughter vessels are assigned to generation *n+1*. In addition, the radius (r; best fit radius averaged over the vessel) and length (l; centerline length) of each vessel were measured. After data acquisition, exponential trend lines were fitted to the data (mean radius, mean length, number of vessels) as a function of the generation number (eq. 1 with *y* the geometrical feature, *x* the generation number; *a* and *b* the coefficients to be fitted). Exponential trend lines were selected, since they showed a better goodness of fit compared to linear and power law trend lines.

$$y(x) = a\, e^{-bx} \tag{1}$$

Mesocirculation

Again, segmentations and 3D reconstructions were performed. As this sample contains vessel generations distal to the macrocirculation, while the resolution is insufficient to capture the microvessels, it is labeled 'mesocirculation'.

Vascular tree analysis of this sample was similar to that of the macrocirculation. However, for labor intensity reasons, we did not analyze the total sample but selected four representative subsamples (brighter subsamples in Fig. 2f-h). To register the mesocirculatory dataset with the macrocirculatory dataset, the ingoing HA, PV and HV vessel of each mesocirculation subsample were identified by their corresponding vessel in the macrocirculatory dataset. Doing so, it was straightforward to assign generation numbers and geometrical feature measurements (radii and lengths) to the mesovessels. However, since we did not quantify the total liver mesovasculature, the number of vessels versus the generation number ($n_{meso,estimated}(x)$; x is the generation number) had to be estimated. This was done by multiplying the measured number of vessels for each

mesocirculation generation ($n_{meso}(x)$) by a factor. This factor is determined by dividing the number of macrocirculation vessels of the f^{th} generation ($n_{macro}(f)$; f is the number of the first mesocirculation generation included in all four subsamples) by the number of measured vessels of generation f in the mesocirculation ($n_{meso}(f)$) (eq. 2).

$$n_{meso,\,estimated}(x) = n_{meso}(x) \cdot \frac{n_{macro}(f)}{n_{meso}(f)} \qquad (2)$$

Microcirculation

Since, at the terminal microcirculation level (interconnected sinusoids), the difference between arterial and portal vessels becomes unclear and the tree structure is lost, the dataset was segmented as one volume, instead of being separated in HA, PV and HV trees. Consequently, this dataset was used to investigate the hepatic vascular microstructure and its dimensions by calculating 3D visualizations and measuring lobule and sinusoid diameters.

Results

The casting procedure resulted in a replica of the human hepatic vascular system (Fig. 1a). HA vessels were red, while PV and HV were blue, due to the relatively high PV flow (75% of the outflow) compared to HA flow, resulting in dominantly blue HV flow.

Macrocirculation

Fig. 2 shows 3D reconstructions of the total liver micro-CT scan. The HA, PV and HV vascular beds were clearly distinguishable. Next to n-furcations (such as bifurcations and trifurcations), the trees count a high number of monopodial vessels, sprouting from parent vessels at angles close to 90° (Fig. 2b-d). After the first generations, HA vessels run parallel to PV vessels. In a few cases, one PV vessel is even flanked by two HA vessels. Moreover, HA vessels have predominantly circular cross-sections compared to elliptical cross-sections of PV and HV vessels. This anatomical feature is probably due to the structural differences between veins (thin vessel walls) and arteries (thick vessel walls including a thick muscle layer). Each tree was classified according to its branching topology, resulting in 6, 6 and 5 generations for the HA, PV and HV tree, respectively. Mean HA radii drop from 3.45 mm to $5.92 \cdot 10^{-1}$ mm, PV radii from 7.34 mm to 1.08 mm and HV radii from 13.2 mm (VCI) to 1.13 mm (Fig. 3a-c; see also Tables 1-4 in (Debbaut et al., 2011)). As anticipated, portal and hepatic venous vessels (PV and HV) have larger diameters compared to HA vessels. Exponential trend lines, fitted to radii measurements, have high determination coefficients ($R^2 \geq 0.97$; see also Tables 1-4 in (Debbaut et al., 2011)). Mean lengths don't show a clear-cut decreasing trend in the first generations (especially for PV vessels), but decrease in higher generations (Fig. 3d-f). This is partially due to the first generation vessel of each tree being cut to resect the liver, implying an underestimated length. Therefore, the

first generation length is not accounted for when calculating length trend lines. The PV length trend line has the lowest R^2 value (0.77). Length standard deviations are higher than for radii. Numbers of vessels per generation clearly increase exponentially towards higher generation numbers: from 1 to 271, 1 to 216, and 1 to 76 vessels for the HA, PV, and HV tree, respectively (Fig. 3g-i; see also Tables 1-4 in (Debbaut et al., 2011)).

Mesocirculation

Segmentations of the mesocirculation subsample (Fig. 1b) were more challenging than the macrocirculation, because more vessels were touching each other (Fig. 2e-h). Fig. 1b and 2e show that the PV inflow runs parallel to two HA vessels. Similar to the macrocirculation, this sample shows elliptical PV and HV vessels compared to circular HA vessels. Analyzing four subsamples (Fig. 2f-h) resulted in the visualization of higher generation vessels, going up to generation 13, 13 and 10 for the HA, PV and HV trees, respectively (Table 1, Fig. 3). Mean radii decrease to $8.00 \cdot 10^{-2}$, $1.23 \cdot 10^{-1}$and $1.60 \cdot 10^{-1}$ mm for the HA, PV and HV trees, respectively (Fig. 3a-c). Radii trend lines were fitted to the pooled macro- and mesocirculation measurements ($R^2 \geq 0.98$). Mean lengths also decrease for all trees ($R^2 \geq 0.94$). The numbers of vessels per generation again increases exponentially, almost exactly following extrapolations of the macrocirculation trend lines. All trend lines fitted to the combination of macro- and mesocirculation measurements show equal or higher goodness of fit than those fitted to only the macrocirculation, except for the HA radii (Fig. 3).

Microcirculation

Scanning electron microscopy of the microcirculation sample shows that casting resin was observed in the sinusoids (Fig. 1c). The sample represents a complex network of interconnected and tortuous sinusoids (Fig. 4). Measurements of one hundred sinusoids resulted in a mean diameter of 13.23 ± 2.36 μm.

283 **Discussion**

284

285 For the first time, the total spectrum of the (human) hepatic vasculature (from the largest vessels
286 down to the sinusoidal microcirculation) is visualized and 3D reconstructed. Therefore, this pilot
287 study used a combination of state-of-the-art vascular corrosion casting and micro-CT scanning
288 techniques (at resolutions up to the order of 2.6 µm) with a novel image processing and analysis
289 technique.

290

291 However, one has to be careful when generalizing these findings based on a single liver because
292 of potential individual differences such as different vessel dimensions, different liver sizes
293 according to the body weight (the liver represents approximately 2% of the total body weight),
294 different liver shapes (e.g. a relatively small or large left lobe) and the potential presence of liver
295 pathology (e.g. fibrotic tissue and regenerative nodules in liver cirrhosis). More livers should thus
296 be similarly analyzed to get a general overview of the human hepatic vascular architecture. As
297 such, this pilot study should be interpreted as the vascular analysis of a specific liver. This human
298 liver was offered to our lab after failed rescue allocation and there was no obvious macroscopic
299 abnormality. The casting procedure was done by manual injection, having the advantage of
300 sensing how the organ reacts while injecting. Also, it has been described that casting may lead to
301 slight shrinkage of the resin, which would imply slightly smaller diameters (Kratky and Roach,
302 1984). However, our diameter measurements were comparable with literature data on the largest
303 hepatic vessels and sinusoidal diameters (Matsumoto and Kawakami, 1982, Warren et al., 2008,
304 Vollmar and Menger, 2009). Moreover, the casting procedure was performed according to
305 standardized procedures by a team having many years of expertise (Debbaut et al., 2011,
306 Casteleyn et al., 2010, Debbaut et al., 2012a).

Ideally, the complete cast should be scanned at once at a sufficiently high resolution to allow visualizing all vessels down to the sinusoids. However, it was technically impossible to scan a total liver at a resolution of a few micrometers due to computational and software limitations to process datasets with an extremely large file size. Consequently, a multiscale approach was used to consecutively study the macro-, meso- and microcirculation, allowing the quantification of 13 (HA and PV) and 10 (HV) blood vessel generations as well as the sinusoids. However, there is still a gap of a number of generations between the $10/13^{th}$ generation and the sinusoids. Nonetheless, the total number of generations can be approximated by extrapolating the resulting exponential trend lines of the radius (Fig. 3) down to the level of radius values of the terminal vessels, resulting in an estimation of 19-20, 17-18 and 13-14 generations for the HA, PV and HV trees, respectively. Hereby, sinusoids are interpreted as being the connection between the terminal/last generation of the inflow trees (HA and PV) and outflow tree (HV).

Our data reveal a complex hepatic vascular topology covering the macro- down to the microcirculation, showing that hepatic trees do not solely branch according to a dichotomous bifurcating pattern, which is often assumed in vascular tree models. *N*-furcations as well as monopodial vessels were clearly visualized in the macro- and mesocirculation. Geometrical characteristics (Fig. 3) show exponential behavior as a function of generation numbers. HA and PV trees show similar behavior and exponential trends, resulting in equal numbers of generations for the macro- and mesocirculation. However, PV radii are larger than HA radii, and starting from generation 4, numbers of HA vessels are higher than those of PV vessels (Fig. 3 g-h, Table 1 and Tables 2-4 in (Debbaut et al., 2011)), probably due to some PV vessels being flanked by two parallel HA vessels. The HV tree has the largest radii and typically counts less generations

than the HA and PV tree.

In contrast, the microcirculation gives evidence of a completely different type of organization compared to vascular trees. Tortuous sinusoids form an interconnected and intertwined network embedded in a matrix of liver cells. Consequently, the exponential behavior of the HA, PV and HV trees probably stops at the level of the terminal microcirculation (where blood is drained from the terminal hepatic arterioles and portal venules into the sinusoids). From our data, macro- and mesovessels may be interpreted as "distributing" vessels, ensuring that blood reaches all liver lobules, and the sinusoids may be interpreted as "functional" vessels, ensuring that blood solutes are able to penetrate through sinusoidal fenestrations into the space of Disse and reach the microvilli of hepatocytes for metabolic exchange. The microvascular sample clearly shows sinusoidal structures (Fig. 1c; meaning that the casting resin was able to fill the sinusoids) and is thought to include three liver lobules. Hereby, the vascular septa of lobules seem to be highlighted by contrast agent particles (bright dots in Fig. 4a). These particles are probably not able to penetrate into the sinusoids because of their size, leaving them trapped at the vascular septa, (partially) delineating the lobule borders (Fig. 4b). Accordingly, the sample represents three liver lobules (Fig. 4a-b) and based on these contours, lobule diameters were in the order of 700-800 µm. As illustrated, it is not obvious to distinguish between neighboring lobules. This might be due to the fact that the human liver microcirculation is characterized by less connective tissue delineating its lobule borders in comparison with pig or rodent livers, often used as animal liver models. Furthermore, lobules can have more irregular shapes than the traditionally hexagonal prism-shaped lobules. Concerning this, literature gives evidence of an ongoing discussion on the most appropriate functional unit to represent the liver microcirculation (e.g. hexagonal lobule, primary lobule, liver acinus) (Roskams et al., 2007).

The novel and detailed morphological data gathered in this study are useful to complement scientific insights into liver morphology and physiology. The new multiscale approach is also applicable in the context of liver pathophysiology, e.g. to investigate pathology-related microvascular alterations in case of fibrosis and cirrhosis (Chen et al., 2009, Vanheule et al., 2008), hepatocellular carcinoma (Maksan et al., 2003), portal hypertension (Fondevila et al., 2010, Yagi et al., 2005). Furthermore, this approach may generate input data for the development of numerical models of liver perfusion. These models can be applied to simulate the hemodynamic impact of (ab)normal situations such as isolated organ perfusion and surgical procedures, e.g. partial hepatectomy. Microcirculation morphological data enable gaining more insight into structural-related characteristics (porosity, permeability tensor) which allow capturing and modeling the microcirculation behavior (especially relevant when studying microvascular alterations caused by e.g. cirrhosis).

Concluding remarks

In conclusion, combining vascular corrosion casting with state-of-the-art high resolution micro-CT scanning provides novel and unique data on the human hepatic vasculature from the macrocirculation down to the microcirculation. A new multiscale approach allows visualizing the complex liver vasculature at different levels in 3D and performing a detailed analysis of the topology and geometrical features. These data are useful to create numerical models of the hepatic blood circulation. This approach could also be applied to other organs, such as kidneys.

Acknowledgements

This research was supported by the Agency for Innovation by Science and Technology in Flanders (IWT), Belgium. Diethard Monbaliu holds a chair of the Centrale Afdeling voor Fractionering (CAF), Vilvoorde, Belgium. There is no conflict of interest.

383 **References**

384

385 Anthony PP, Ishak KG, Nayak NC, Poulsen HE, Scheuer PJ, Sobin LH (1978) Morphology of
386 cirrhosis. *Journal of Clinical Pathology,* **31,** 395-414.
387 Bonfiglio A, Leungchavaphongse K, Repetto R, Siggers JH (2010) Mathematical modeling of the
388 circulation in the liver lobule. *Journal of Biomechanical Engineering,* **132,** 111011.
389 Casteleyn C, Trachet B, Van Loo D, et al. (2010) Validation of the murine aortic arch as a model
390 to study human vascular diseases. *Journal of Anatomy,* **216,** 563-571.
391 Chen ML, Zeng QY, Huo JW, Yin XM, Li BP, Liu JX (2009) Assessment of the hepatic
392 microvascular changes in liver cirrhosis by perfusion computed tomography. *World*
393 *Journal of Gastroenterology,* **15,** 3532-3537.
394 Debbaut C, De Wilde D, Casteleyn C, et al. (2012a) Modeling the Impact of Partial Hepatectomy
395 on the Hepatic Hemodynamics Using a Rat Model. *Ieee Transactions on Biomedical*
396 *Engineering,* **59,** 3293-3303.
397 Debbaut C, Monbaliu D, Casteleyn C, et al. (2011) From vascular corrosion cast to electrical
398 analog model for the study of human liver hemodynamics and perfusion. *IEEE*
399 *Transactions on Biomedical Engineering,* **58,** 25-35.
400 Debbaut C, Vierendeels J, Casteleyn C, et al. (2012b) Perfusion characteristics of the human
401 hepatic microcirculation based on three-dimensional reconstructions and computational
402 fluid dynamic analysis. *Journal of Biomechanical Engineering,* **134**.
403 Eipel C, Abshagen K, Vollmar B (2010) Regulation of hepatic blood flow: The hepatic arterial
404 buffer response revisited. *World Journal of Gastroenterology,* **16,** 6046-6057.

405 Ekataksin W, Wake K (1991) Liver units in 3 dimensions: 1. Organization of argyrophilic
406 connective-tissue skeleton in porcine liver with particular reference to the compound
407 hepatic lobule. *American Journal of Anatomy,* **191,** 113-153.
408 Ekataksin W, Wake K (1997) New concepts in biliary and vascular anatomy of the liver.
409 *Progress in Liver Diseases* **15,** 1-30.
410 Finet G, Gilard M, Perrenot B, et al. (2007) Fractal geometry of arterial coronary bifurcations: a
411 quantitative coronary angiography and intravascular ultrasound analysis. *EuroInvention,*
412 **3,** 490-498.
413 Fondevila C, Hessheimer AJ, Taura P, et al. (2010) Portal hyperperfusion: mechanism of injury
414 and stimulus for regeneration in porcine small-for-size transplantation. *Liver*
415 *Transplantation,* **16,** 364-374.
416 Francque S, Laleman W, Verbeke L, et al. (2012) Increased intrahepatic resistance in severe
417 steatosis: endothelial dysfunction, vasoconstrictor overproduction and altered
418 microvascular architecture. *Laboratory Investigation,* **92,** 1428-1439.
419 Gomes RFM, Bates JHT (2002) Geometric determinants of airway resistance in two isomorphic
420 rodent species. *Respiratory Physiology & Neurobiology,* **130,** 317-325.
421 Gordon Z, Elad D, Almog R, Hazan Y, Jaffa AJ, Eytan O (2007) Anthropometry of fetal
422 vasculature in the chorionic plate. *Journal of Anatomy,* **211,** 698-706.
423 Greenway CV, Stark RD (1971) Hepatic vascular bed. *Physiological Reviews,* **51,** 23-65.
424 Kratky RG, Roach MR (1984) Shrinkage of Batsons and its relevance to vascular casting.
425 *Atherosclerosis,* **51,** 339-341.
426 Maksan SM, Paulo H, Ryschich E, et al. (2003) In vivo assessment of angioarchitecture and
427 microcirculation in experimental liver cancer - a new model in rats. *Digestive Diseases*
428 *and Sciences,* **48,** 279-290.

429 Matsumoto T, Kawakami M (1982) The unit-concept of hepatic parenchyma - a re-examination
430 based on angioarchitectural studies. *Acta Pathologica Japonica,* **32,** 285-314.
431 Matsumoto T, Komori R, Magara T, et al. (1979) A study on the normal structure of the human
432 liver, with special reference to its angioarchitecture. *Jikeikai Medical* **26,** 1-40.
433 McCuskey RS (1966) A dynamic and static study of hepatic arterioles and hepatic sphincters.
434 *American Journal of Anatomy,* **119,** 455-477.
435 McCuskey RS, Reilly FD (1993) Hepatic microvasculature: dynamic structure and its regulation.
436 *Seminars in Liver Disease,* **13,** 1-12.
437 Monbaliu D, Debbaut C, Hillewaert W, et al. (2012) Flow competition between hepatic arterial
438 and portal venous flow during hypothermic machine perfusion preservation of porcine
439 livers. *International Journal of Artificial Organs,* **35,** 119-131.
440 Mutter D, Dallemagne B, Bailey C, Soler L, Marescaux J (2009) 3D virtual reality and selective
441 vascular control for laparoscopic left hepatic lobectomy. *Surgical Endoscopy and Other*
442 *Interventional Techniques,* **23,** 432-435.
443 Op Den Buijs JB, Z., Ritman EL (2006) Branching morphology of the rat hepatic portal vein tree:
444 a micro-CT study. *Annals of Biomedical Engineering,* **34,** 1420-1428.
445 Rani HP, Sheu TWH, Chang TM, Liang PC (2006) Numerical investigation of non-Newtonian
446 microcirculatory blood flow in hepatic lobule. *Journal of Biomechanics,* **39,** 551-563.
447 Rappaport AM, Borowy ZJ, Lougheed WM, Lotto WN (1954) Subdivision of hexagonal liver
448 lobules into a structural and functional unit; role in hepatic physiology and pathology.
449 *Anatomical record,* **119,** 11-33.
450 Rennie MY, Detmar J, Whiteley KJ, et al. (2011) Vessel tortuousity and reduced vascularization
451 in the fetoplacental arterial tree after maternal exposure to polycyclic aromatic

hydrocarbons. *American Journal of Physiology-Heart and Circulatory Physiology,* **300,** H675-H684.

Ricken T, Dahmen U, Dirsch O (2010) A biphasic model for sinusoidal liver perfusion remodeling after outflow obstruction. *Biomechanics and Modeling in Mechanobiology,* **9,** 435-450.

Roskams T, Desmet VJ, Verslype C (2007) Development, structure and function of the liver. In *MacSween's Pathology of the liver* (eds Burt AD, Portmann BC, Ferrell LD), pp. 1-72. Churchill Livingstone.

Selle D, Preim B, Schenk A, Peitgen H-O (2002) Analysis of vasculature for liver surgical planning. *Ieee Transactions on Medical Imaging,* **21,** 1344-1357.

Teutsch HF (2005) The modular microarchitecture of human liver. *Hepatology,* **42,** 317-325.

Teutsch HF, Schuerfeld D, Groezinger E (1999) Three-dimensional reconstruction of parenchymal units in the liver of the rat. *Hepatology,* **29,** 494-505.

Thabut D, Shah V (2010) Intrahepatic angiogenesis and sinusoidal remodeling in chronic liver disease: New targets for the treatment of portal hypertension? *Journal of Hepatology,* **53,** 976-980.

Vanheule E, Geerts AM, Van Huysse J, et al. (2008) An intravital microscopic study of the hepatic microcirculation in cirrhotic mice models: relationship between fibrosis and angiogenesis. *International Journal of Experimental Pathology,* **89,** 419-432.

Vollmar B, Menger MD (2009) The hepatic microcirculation: mechanistic contributions and therapeutic targets in liver injury and repair. *Physiological Reviews,* **89,** 1269-1339.

Wagner R, Van Loo D, Hossler F, Czymmek K, Pauwels E, Van Hoorebeke L (2011) High-resolution imaging of kidney vascular corrosion casts with nano-CT. *Microscopy and Microanalysis,* **17,** 215-219.

476 Warren A, Chaberek S, Ostrowski K, et al. (2008) Effects of old age on vascular complexity and
477 dispersion of the hepatic sinusoidal network. *Microcirculation,* **15,** 191-202.
478 Yagi S, Lida T, Taniguchi K, et al. (2005) Impact of portal venous pressure on regeneration and
479 graft damage after living-donor liver transplantation. *Liver Transplantation,* **11,** 68-75.
480 Yamanaka J, Saito S, Iimuro Y, et al. (2006) The impact of 3-D virtual hepatectomy simulation
481 in living-donor liver transplantation. *Journal of Hepato-Biliary-Pancreatic Surgery*, **13,**
482 363-369.

483

484

485 **Tables**

486 **Table 1. Overview of the mesoscale HA, PV and HV measurements.** Mean radii, mean
487 lengths and numbers of vessels are reported per generation number. (Estimated numbers of
488 vessels of mesocirculation generations are calculated using eq. 2.)

	Generation number	Mean radius [mm]	Standard deviation of radius [mm]	Mean length [mm]	Standard deviation of length [mm]	Number of vessels	Estimated number of vessels
HA Mesoscale	HA 5	$8.62 \cdot 10^{-1}$	$3.54 \cdot 10^{-3}$	54.4	25.4	2	
	HA 6	$5.21 \cdot 10^{-1}$	$1.54 \cdot 10^{-1}$	12.2	8.29	6	
	HA 7	$3.45 \cdot 10^{-1}$	$3.90 \cdot 10^{-2}$	7.22	4.04	12	542
	HA 8	$2.77 \cdot 10^{-1}$	$4.70 \cdot 10^{-2}$	3.51	2.62	34	1536
	HA 9	$2.41 \cdot 10^{-1}$	$4.19 \cdot 10^{-2}$	3.09	2.08	76	3433
	HA 10	$2.08 \cdot 10^{-1}$	$2.73 \cdot 10^{-2}$	2.36	1.38	198	8943
	HA 11	$1.60 \cdot 10^{-1}$	$2.62 \cdot 10^{-2}$	1.48	1.05	342	15447
	HA 12	$1.19 \cdot 10^{-1}$	$2.47 \cdot 10^{-2}$	1.00	$5.45 \cdot 10^{-1}$	225	10163
	HA 13	$8.00 \cdot 10^{-2}$	$2.46 \cdot 10^{-2}$	$7.41 \cdot 10^{-1}$	$2.40 \cdot 10^{-1}$	9	407
PV Mesoscale	PV 5	1.41	0	19.9	0	1	
	PV 6	$8.86 \cdot 10^{-1}$	$2.25 \cdot 10^{-1}$	14.8	7.94	5	
	PV 7	$7.18 \cdot 10^{-1}$	$1.72 \cdot 10^{-1}$	8.14	4.33	10	432
	PV 8	$4.82 \cdot 10^{-1}$	$1.12 \cdot 10^{-1}$	5.24	2.80	31	1339
	PV 9	$3.09 \cdot 10^{-1}$	$6.16 \cdot 10^{-2}$	3.16	1.80	86	3715
	PV 10	$2.31 \cdot 10^{-1}$	$3.92 \cdot 10^{-2}$	2.68	1.39	244	10541
	PV 11	$1.75 \cdot 10^{-1}$	$2.61 \cdot 10^{-2}$	1.48	$8.75 \cdot 10^{-1}$	555	23976
	PV 12	$1.38 \cdot 10^{-1}$	$2.39 \cdot 10^{-2}$	1.03	$4.91 \cdot 10^{-1}$	73	3154
	PV 13	$1.23 \cdot 10^{-1}$	$2.71 \cdot 10^{-2}$	$9.50 \cdot 10^{-1}$	$3.79 \cdot 10^{-1}$	6	259
HV Mesoscale	HV 5	1.27	$4.42 \cdot 10^{-1}$	32.5	12.7	4	
	HV 6	$7.41 \cdot 10^{-1}$	$9.27 \cdot 10^{-2}$	8.56	5.30	9	171
	HV 7	$4.56 \cdot 10^{-1}$	$9.66 \cdot 10^{-2}$	6.59	3.23	26	494
	HV 8	$2.46 \cdot 10^{-1}$	$7.65 \cdot 10^{-2}$	4.09	1.97	111	2109
	HV 9	$1.71 \cdot 10^{-1}$	$5.59 \cdot 10^{-2}$	2.61	1.47	74	1406
	HV 10	$1.60 \cdot 10^{-1}$	$6.10 \cdot 10^{-2}$	2.17	1.06	20	380

489

Figure legends

Figure 1. Human liver vascular corrosion cast and micro-CT scanner. (A) Total liver with indication of the dissection location of the mesocirculation sample; (B) mesocirculation sample; (C) scanning electron microscopic image of the microcirculation sample; (D) micro-CT scanner with a static X-ray tube, a static flat panel detector and a rotating liver cast to capture images during a 360° rotation.

Figure 2. 3D reconstructions of the macrocirculation and mesocirculation. (A) Superposition of three macrovascular trees with indication of the dissection location of the mesocirculation sample; macrovascular HA (B), PV (C) and HV trees (D) with arrows indicating monopodial branches; (E) superposition of three mesovascular trees; mesovascular HA (F), PV (G) and HV trees (H) with brighter parts indicating four subsamples used to acquire geometrical data.

Figure 3. Results of the vascular tree analysis of the macro- and mesocirculation. Radius (A-C), length (D-F) and number of vessels (G-I) as a function of the generation number for the HA, PV and HV trees. Macro-circulation measurements (as obtained in (Debbaut et al., 2011)) and mesocirculation measurements are indicated by black and white markers, respectively. (Original and estimated numbers of vessels for the mesocirculation (Table 1) are indicated by gray and white dots, respectively). Exponential trend lines are depicted by dashed lines when fitted to macro- and mesocirculation data. Equations and coefficients of determination (R^2) of the exponential functions are given. The first HV generation (VCI) was not taken into accounted when fitting the radius trend line, since the VCI has a much larger diameter and is not really part

511 of the hepatic vasculature. Length trend lines did not incorporate the first generation, since these
512 vessels were cut to resect the liver, resulting in an underestimated length.

513 **Figure 4. Liver microcirculation.** (A) Single micro-CT slice showing bright spots (probably
514 contrast agent particles); (B) indication of the most likely lobule borders; (C) 3D reconstruction
515 of the microcirculation sample and (D) of a virtually dissected cubic subsample.

516

Figures

Figure 1.

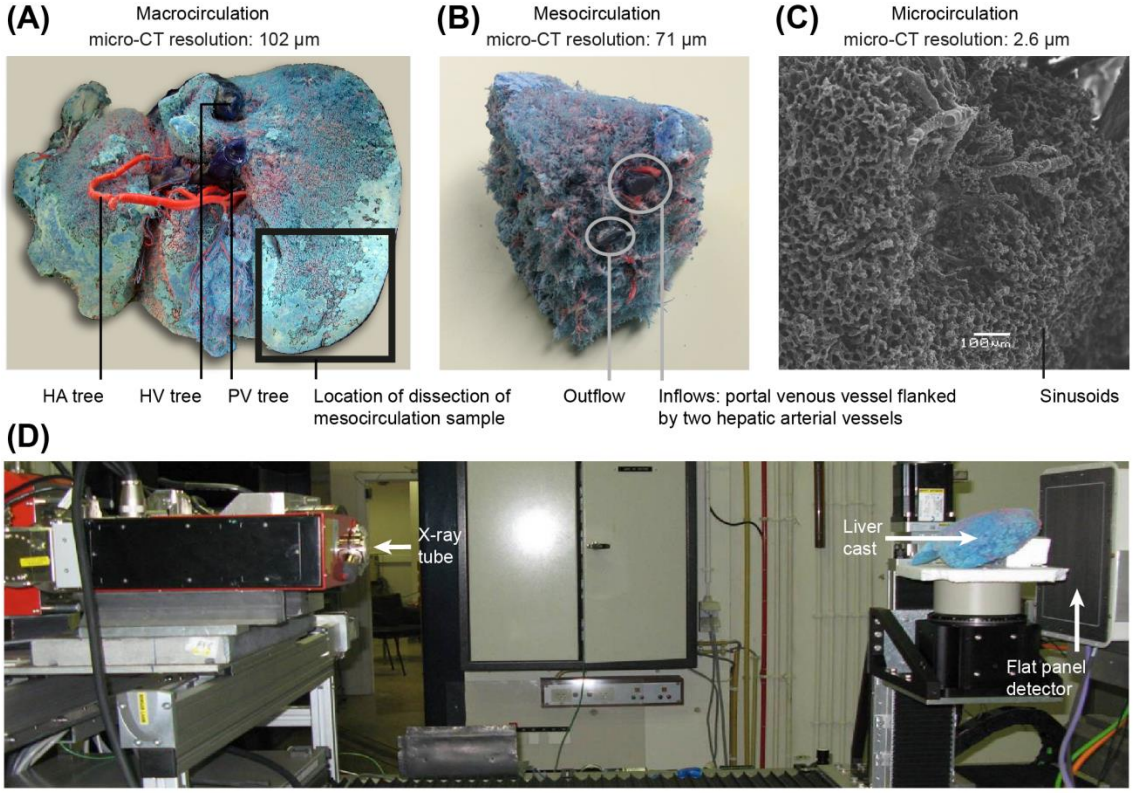

Figure 2.

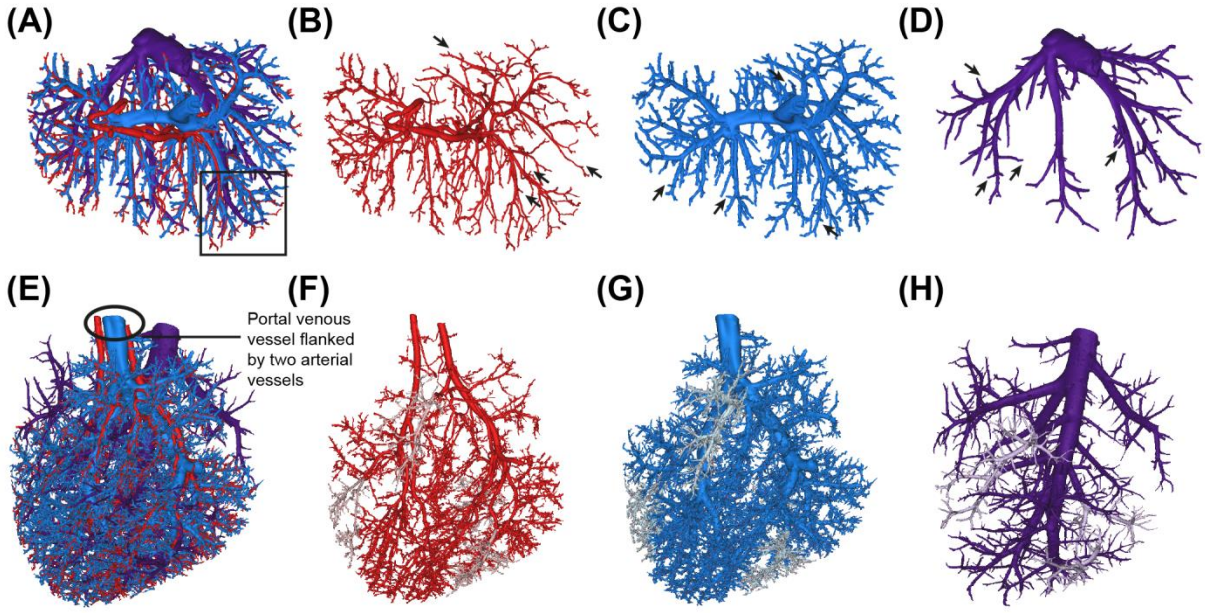

Figure 3.

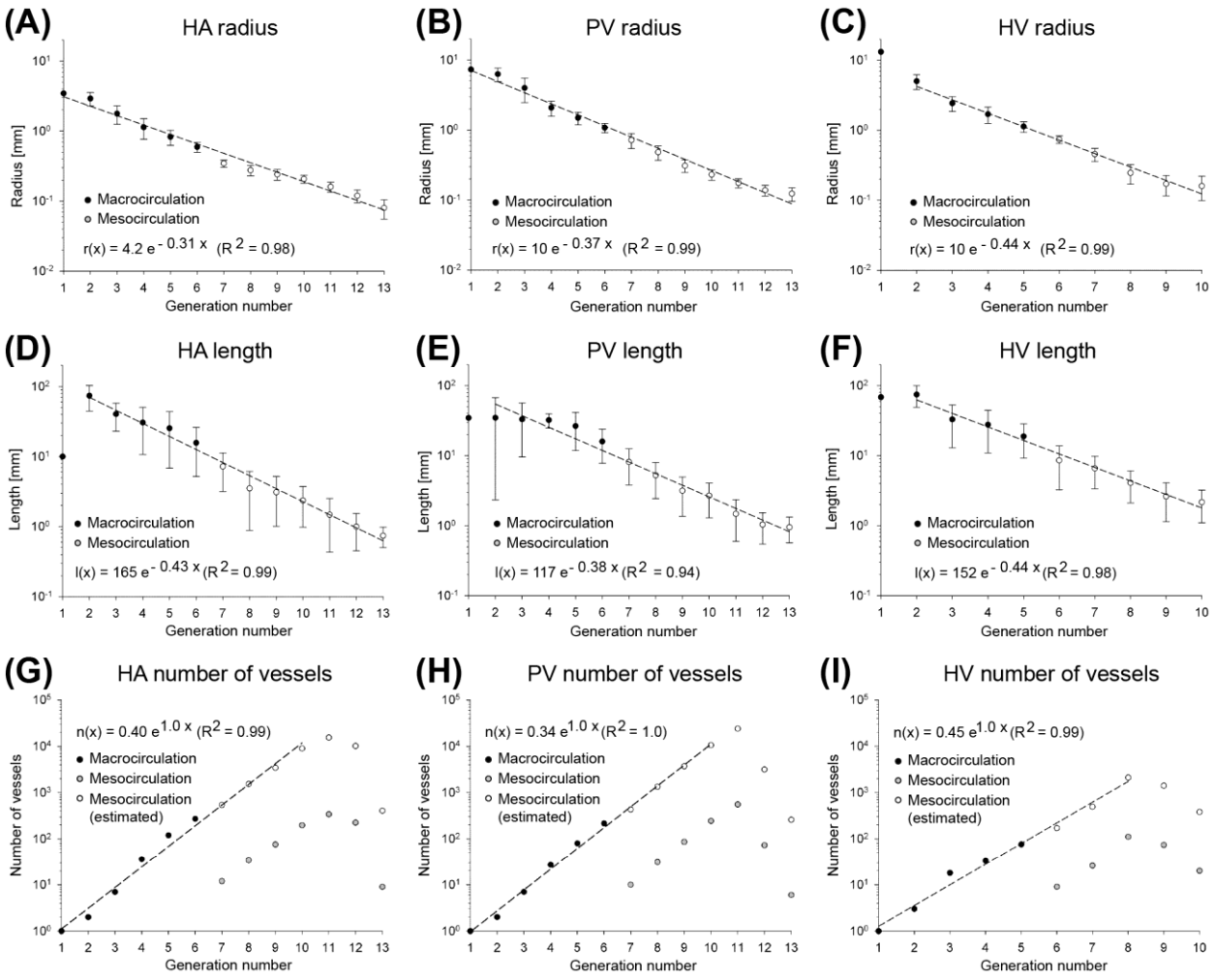
(A)
HA radius
Radius [mm]
Macrocirculation
Mesocirculation
r(x) = 4.2 e - 0.31 x (R 2 = 0.98)
Generation number
(B)
PV radius
Radius [mm]
Macrocirculation
Mesocirculation
r(x) = 10 e - 0.37 x (R 2 = 0.99)
Generation number
(C)
HV radius
Radius [mm]
Macrocirculation
Mesocirculation
r(x) = 10 e - 0.44 x (R 2 = 0.99)
Generation number
(D)
HA length
Length [mm]
Macrocirculation
Mesocirculation
l(x) = 165 e - 0.43 x (R 2 = 0.99)
Generation number
(E)
PV length
Length [mm]
Macrocirculation
Mesocirculation
l(x) = 117 e - 0.38 x (R 2 = 0.94)
Generation number
(F)
HV length
Length [mm]
Macrocirculation
Mesocirculation
l(x) = 152 e - 0.44 x (R 2 = 0.98)
Generation number
(G)
HA number of vessels
n(x) = 0.40 e 1.0 x (R 2 = 0.99)
Number of vessels
Macrocirculation
Mesocirculation
Mesocirculation (estimated)
Generation number
(H)
PV number of vessels
n(x) = 0.34 e 1.0 x (R 2 = 1.0)
Number of vessels
Macrocirculation
Mesocirculation
Mesocirculation (estimated)
Generation number
(I)
HV number of vessels
n(x) = 0.45 e 1.0 x (R 2 = 0.99)
Number of vessels
Macrocirculation
Mesocirculation
Mesocirculation (estimated)
Generation number

527 **Figure 4.**

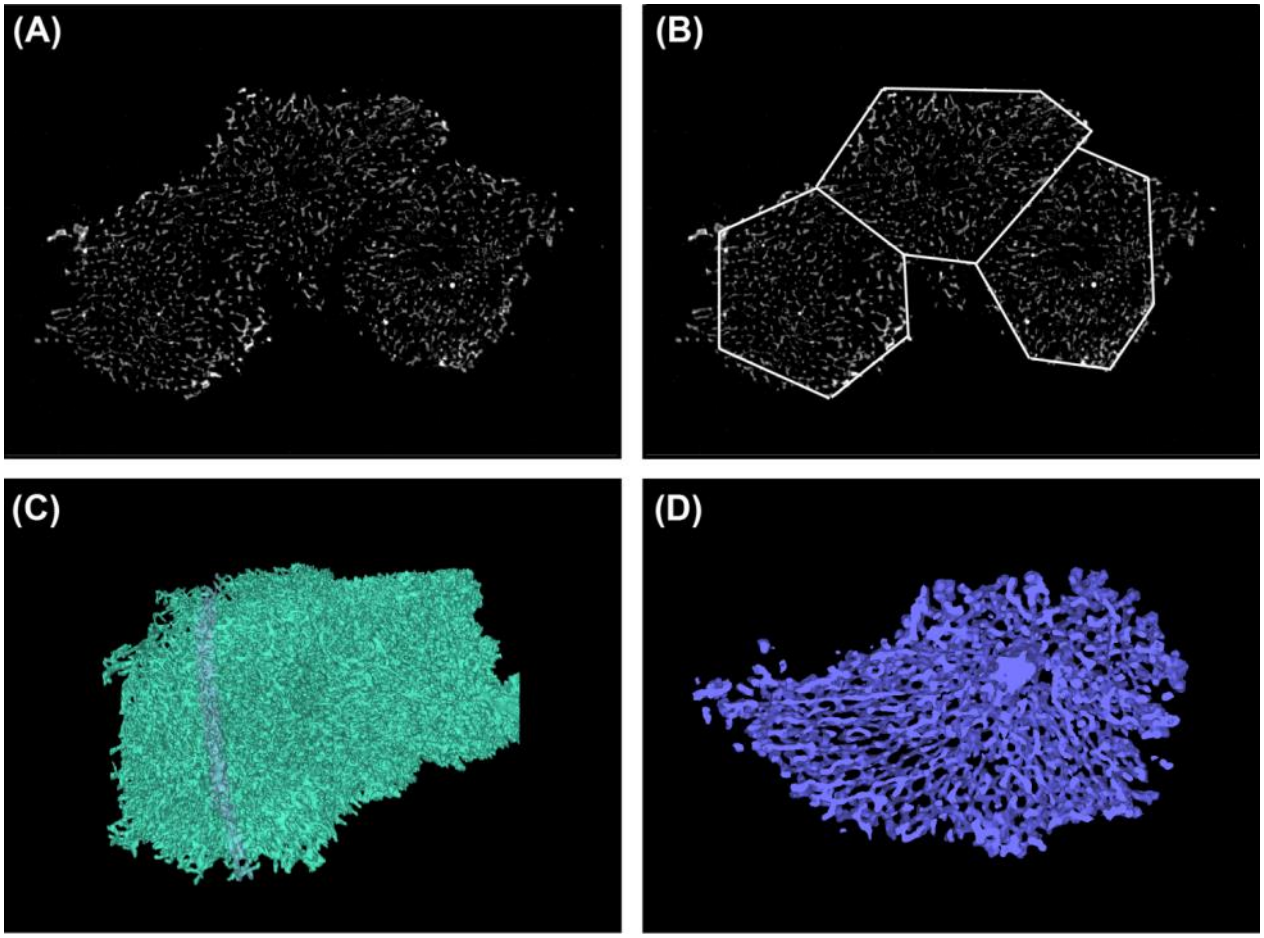

528

529